

LETTER TO THE EDITOR

Water in low-mass star-forming regions with *Herschel*[★] (WISH-LM)

High-velocity H₂O bullets in L1448-MM observed with HIFI^{★★}

L. E. Kristensen¹, E. F. van Dishoeck^{1,2}, M. Tafalla³, R. Bachiller³, B. Nisini⁴, R. Liseau⁵, and U. A. Yıldız¹

¹ Leiden Observatory, Leiden University, PO Box 9513, 2300 RA Leiden, The Netherlands
e-mail: Kristensen@strw.leidenuniv.nl

² Max Planck Institut für Extraterrestrische Physik, Giessenbachstrasse 1, 85748 Garching, Germany

³ Observatorio Astronómico Nacional (IGN), Calle Alfonso XII, 3. 28014 Madrid, Spain

⁴ INAF - Osservatorio Astronomico di Roma, 00040 Monte Porzio catone, Italy

⁵ Department of Earth and Space Sciences, Chalmers University of Technology, Onsala Space Observatory, 439 92 Onsala, Sweden

Received 29 March 2011 / Accepted 18 May 2011

ABSTRACT

Herschel-HIFI observations of water in the low-mass star-forming object L1448-MM, known for its prominent outflow, are presented, as obtained within the “Water in star-forming regions with *Herschel*” (WISH) key programme. Six H₂¹⁶O lines are targeted and detected ($E_{\text{up}}/k_{\text{B}} \sim 50\text{--}250$ K), as is CO $J = 10\text{--}9$ ($E_{\text{up}}/k_{\text{B}} \sim 305$ K), and tentatively H₂¹⁸O $1_{10}\text{--}1_{01}$ at 548 GHz. All lines show strong emission in the “bullets” at $|v| > 50$ km s⁻¹ from the source velocity, in addition to a broad, central component and narrow absorption. The bullets are seen much more prominently in H₂O than in CO with respect to the central component, and show little variation with excitation in H₂O profile shape. Excitation conditions in the bullets derived from CO lines imply a temperature >150 K and density $>10^5$ cm⁻³, similar to that of the broad component. The H₂O/CO abundance ratio is similar in the “bullets” and the broad component, $\sim 0.05\text{--}1.0$, in spite of their different origins in the molecular jet and the interaction between the outflow and the envelope. The high H₂O abundance indicates that the bullets are H₂ rich. The H₂O cooling in the “bullets” and the broad component is similar and higher than the CO cooling in the same components. These data illustrate the power of *Herschel*-HIFI to disentangle different dynamical components in low-mass star-forming objects and determine their excitation and chemical conditions.

Key words. astrochemistry – stars: formation – ISM: molecules – ISM: jets and outflows – ISM: individual objects: L1448

1. Introduction

Low-mass star formation is accompanied by the launch of powerful jets that drive strong shocks into the parental material (e.g., Arce et al. 2007), both in the form of shell shocks that interact with the molecular envelope, and in the form of the jet itself (e.g., Hirano et al. 2010). The jets are generally not uniform, but consist of small condensations (“bullets”¹), that can be attributed to internal working surfaces caused by episodic ejection of material from the protostar (Santiago-García et al. 2009). The bullets are chemically rich, in particular in oxygen-bearing species (Tafalla et al. 2010), and should therefore display high abundances of water. H₂O is one of the best shock tracers because the abundance can increase by orders of magnitude up to $\lesssim 10^{-4}$ through sputtering of grain mantles and formation in the gas phase at high temperatures (Flower & Pineau des Forêts 2010). Also, due to the large velocity gradients in shocks, emission is effectively optically thinner than in a quiescent object (Franklin et al. 2008).

H₂O has previously been observed in outflowing gas from young stellar objects (YSOs) using, e.g., *Odin*, SWAS, and ISO. The Heterodyne Instrument for the Far-Infrared (HIFI) on *Herschel* opens up spectrally resolved, high angular resolution

observations of both H₂O and high- J CO in low-mass protostars (e.g., Lefloch et al. 2010; Yıldız et al. 2010; Kristensen et al. 2010). The latter paper presents H₂O observations of the low-mass star-forming region NGC1333. The H₂O line profiles are complex, consisting of three velocity components characterised by their width. The broadest component ($\Delta v > 20$ km s⁻¹) originates in the interaction between the outflow and the envelope; the medium-broad component ($5 < \Delta v < 20$ km s⁻¹) arises where the jet impacts on the inner, dense envelope; a narrow absorption component ($\Delta v < 5$ km s⁻¹) is attributed to the cold outer envelope. These initial HIFI results show that H₂O is one of the best dynamics tracers in YSOs, and confirm that the H₂O/CO abundance increases with velocity to ~ 1 . To date, H₂O has not been uniquely identified in the bullets, and its abundance with respect to other jet species is unknown. Moreover, the different nature of the shocks could lead to different H₂O abundances.

L1448-MM is a low-mass, Class 0 protostar located in Perseus ($L = 11.6 L_{\odot}$, $M_{\text{env}} = 1.9 M_{\odot}$, $d = 235$ pc; van Dishoeck et al. 2011). This object is the prototype of the class of sources showing bullet emission in CO (Bachiller et al. 1990), with red- and blue-shifted emission peaks at $\sim \pm 50$ km s⁻¹ with respect to $v_{\text{LSR}} = +5.2$ km s⁻¹. The bullets are clearly visible in other shock tracers such as SiO (e.g. Nisini et al. 2007), and have been imaged at high spatial resolution using interferometers (e.g., Guilloteau et al. 1992; Hirano et al. 2010). Our observations of H₂O within the framework of the “Water in star-forming regions with *Herschel*” (WISH; van Dishoeck et al. 2011) key

[★] *Herschel* is an ESA space observatory with science instruments provided by European-led Principal Investigator consortia and with important participation from NASA.

^{★★} Appendices and Tables 2 and 3 are available in electronic form at <http://www.aanda.org>

¹ Bullets and extremely high-velocity (EHV) gas are used interchangeably throughout.

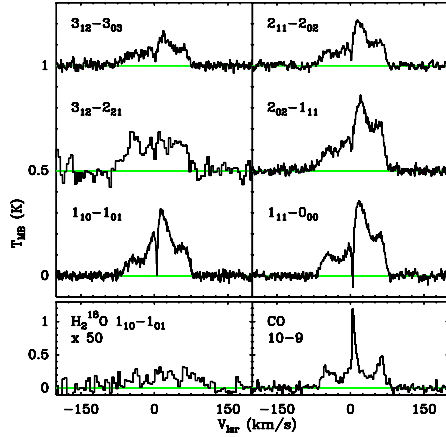


Fig. 1. Continuum-subtracted HIFI H_2O , H_2^{18}O and CO spectra obtained at the central position of L1448-MM ($v_{\text{source}} = 5.2 \text{ km s}^{-1}$).

programme further explore the chemical and excitation conditions of shocked gas in low-mass star-forming regions.

2. Observations and results

The central position of L1448-MM ($03^{\text{h}}25^{\text{m}}38^{\text{s}}.9; +30^{\circ}44'05''.4$; J2000) was observed with HIFI on *Herschel* (de Graauw et al. 2010, Pilbratt et al. 2010) in seven different settings covering six H_2^{16}O , two H_2^{18}O and one CO transition ($E_{\text{u}}/k_{\text{B}} \approx 50\text{--}300 \text{ K}$; Table 3). Data were obtained using the dual beam-switch mode with a nod of $3'$, except for the ground-state ortho- H_2O line at 557 GHz, where a position switch to $(+10'; +5')$ was used. The diffraction-limited beam size ranges from $19''$ to $39''$ (4500–9500 AU). Data were reduced using HIPE ver. 4.0. The calibration uncertainty is taken to be 10% for lines observed in Bands 1, 2, and 5 while it is 30% in Band 4. The pointing accuracy is $\sim 2''$. A main-beam efficiency of 0.65–0.75 is adopted (Table 3). Subsequent analysis of the data is performed in CLASS including subtraction of linear baselines. H- and V-polarizations are co-added after inspection; no significant differences are found between the two data sets. ^{12}CO 3–2 and ^{13}CO 3–2 were observed with the *James Clerk Maxwell Telescope* (JCMT). CO 2–1 was observed at the IRAM 30 m (Tafalla et al. 2010), and CO 4–3 at the JCMT (Nisini et al. 2000).

All targeted lines are detected, except H_2^{18}O $1_{11}\text{--}0_{00}$, observed with the main isotopologue (Fig. 1). This figure strikingly demonstrates that the bullets are much more prominent in H_2O than in CO relative to the central component. Also, the H_2O profiles are very different from those seen in NGC 1333 (Kristensen et al. 2010). Each line consists of multiple components: two Gaussian peaks at velocities of $\sim \pm 50 \text{ km s}^{-1}$ with respect to v_{source} ; a broad ($\sim 50 \text{ km s}^{-1}$) component centered close to v_{source} ; and a narrow ($\sim 5 \text{ km s}^{-1}$) component seen in absorption at v_{source} . The extremely high- v emission (henceforth *EHV* – B and *EHV* – R) is detected in all lines, although the detection in the H_2^{18}O $1_{10}\text{--}1_{01}$ line is tentative (2σ ; 0.13 K km s^{-1}). The emission components are well reproduced by Gaussians and fitted to obtain the integrated intensity (Table 1). The H_2O line profiles vary little with excitation. The shape of the *EHV* component in the CO profiles resembles that of H_2O (Fig. A.1, Appendix), whereas the broad component is much weaker in CO. The CO lines also contain a narrower component ($\sim 10 \text{ km s}^{-1}$) not seen in H_2O .

To compare observations done with different beam sizes, all observations are scaled to a common beam of $22''$, the beam at 988 GHz. The scaling follows the recipe outlined in Appendix B

Table 1. H_2O , H_2^{18}O and CO emission in each velocity component^a.

Transition	rms ^b (mK)	<i>EHV</i> – B $\int T_{\text{MB}} dv$ (K km s^{-1})	<i>EHV</i> – R $\int T_{\text{MB}} dv$ (K km s^{-1})	Broad $\int T_{\text{MB}} dv$ (K km s^{-1})
H_2O $1_{10}\text{--}1_{01}$	9	2.54	3.00	14.4
$1_{11}\text{--}0_{00}$	11	3.98	4.00	14.8
$2_{02}\text{--}1_{11}$	14	4.01	3.86	17.6
$2_{11}\text{--}2_{02}$	14	2.47	2.53	9.9
$3_{12}\text{--}3_{03}$	13	2.34	1.14	7.8
$3_{12}\text{--}2_{21}$	66	6.22	3.32	7.9
H_2^{18}O $1_{10}\text{--}1_{01}$ ^c	3	0.13	0.11	0.23
$1_{11}\text{--}0_{00}$ ^d	11	<0.25	<0.19	<0.28
CO 2–1	51	2.79	4.12	38.5
3–2	39	4.82	6.58	44.9
4–3	160	11.9	15.1	74.6
10–9	66	7.30	8.42	17.8
<i>FWHM</i> ^e (km s^{-1})		38.4 ± 3.2	22.4 ± 3.0	47.6 ± 4.5
v_{LSR} ^e (km s^{-1})		-43.4 ± 1.3	59.3 ± 1.8	16.8 ± 2.2

Notes. (a) Obtained from Gaussian fits to each component. All Gaussian fit parameters are provided in Table 2. (b) Measured in 1 km s^{-1} bins. (c) Obtained by fixing the position and width of Gaussian functions and only fitting the intensity. (d) Upper limits are 3σ . (e) Intensity-weighted average of values determined from Gaussian fits to the H_2O lines. Uncertainties include statistical errors only.

of Tafalla et al. (2010), where a linear scaling with beam size is found to be appropriate for the *EHV* components and a power-law scaling with index 0.75 for the broad component. It is only significant for the 557 GHz lines due to the larger beam ($39''$).

The tentative detection of the H_2^{18}O $1_{10}\text{--}1_{01}$ (548 GHz) line is used to constrain the optical depth, τ , of the main isotopologue, assuming that the line itself is optically thin and that $[\text{H}_2^{16}\text{O}]/[\text{H}_2^{18}\text{O}] = 550$. The optical depth, τ , is ~ 25 in each *EHV* component and 9 in the broad component implying that emission from H_2^{16}O $1_{10}\text{--}1_{01}$ is optically thick. The 3σ upper limit on the H_2^{18}O $1_{11}\text{--}0_{00}$ line implies $\tau \lesssim 10$ and $\lesssim 30$ in H_2^{16}O for the broad and *EHV* components, respectively. ^{13}CO 3–2 emission is not detected in any of the components. The ^{12}CO 3–2 optical depth is $\lesssim 2$ and $\lesssim 0.3$ in the *EHV* and broad components, respectively, implying that the CO emission is optically thin.

The integrated intensities of each of the *EHV* and broad components are used to construct Boltzmann diagrams, where the column density of each upper level in the optically thin limit (N_{up}^*) per sub-level is plotted versus E_{up} (Fig. 2). In the diagrams, N_{up}^* for the H_2O ground-state transitions is lower than expected, confirming that the true N_{up} is higher and that the lines are optically thick. Excluding these two lines from further analysis, the resulting rotational temperature is remarkably similar for all three components ($\sim 45\text{--}60 \text{ K}$), while the beam-averaged column density of the broad component is ~ 5 times higher than that of the *EHV* components (~ 10 and $2 \times 10^{13} \text{ cm}^{-2}$, respectively; Table 4). Rotational diagrams are also made for CO and results are given in Table 4. T_{rot} is significantly higher, 150 K in the *EHV* components and 80 K in the broad. The column density is also higher, $\sim 10^{16} \text{ cm}^{-2}$, and the inferred $\text{H}_2\text{O}/\text{CO}$ ratio is ~ 0.002 .

3. Discussion

3.1. Excitation conditions

To determine the physical parameters, a small grid of RADEX slab models was run (van der Tak et al. 2007). This grid is first used to determine CO excitation conditions by fitting T_{rot} (see Fig. B.1 in Appendix B). To reproduce $T_{\text{rot}} \sim 150 \text{ K}$ as observed in the *EHV* components, a kinetic temperature of 150 K and density greater than $\sim 10^6 \text{ cm}^{-3}$ is required. Alternatively, a kinetic

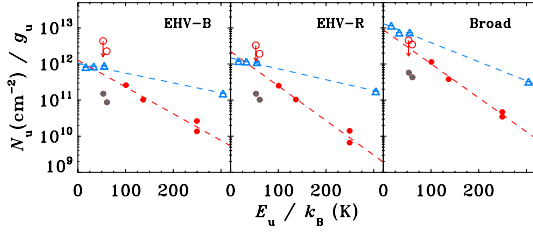


Fig. 2. Rotational diagrams of the *EHV* and broad components for H_2O (red circles) and CO (blue triangles). CO has been shifted downwards by a factor of 100. The ground-state transitions (grey) are excluded from the fit (dashed lines). H_2^{18}O intensities $\times 550$ are shown as open circles.

Table 4. Rotational-diagram results for each velocity component.

Component	H_2O		CO	
	T_{rot} (K)	N (10^{13} cm^{-2})	T_{rot} (K)	N (10^{15} cm^{-2})
<i>EHV</i> - <i>B</i>	58 ± 4	1.9 ± 0.4	160 ± 18	6.0 ± 0.7
<i>EHV</i> - <i>R</i>	45 ± 3	2.4 ± 0.5	144 ± 14	7.6 ± 0.8
Broad	46 ± 2	9.5 ± 2.1	82 ± 4	38.6 ± 3.9

temperature of ~ 500 K and density of $\sim 10^5 \text{ cm}^{-3}$ can also reproduce the observed CO rotational temperature. In the following, both sets of values, $(T, n) = (150 \text{ K}, 10^6 \text{ cm}^{-3})$; model 1), and $(500 \text{ K}, 10^5 \text{ cm}^{-3})$; model 2), will be examined to constrain the H_2O excitation. Similar values are needed to reproduce the lower CO rotational temperature of the broad component, $T_{\text{rot}} \sim 80$ K, $(T, n) = (100 \text{ K}, 10^6 \text{ cm}^{-3})$ and $(500 \text{ K}, 5 \times 10^4 \text{ cm}^{-3})$. The latter solution is excluded, however, because the envelope density within the $20''$ beam is always $> 4 \times 10^5 \text{ cm}^{-3}$. Independent analysis of outflow emission (Nisini et al. 1999; Nisini et al. 2000) indicate that H_2O is excited in a hotter, denser medium than CO , and for this reason a model with $(T, n) = (500 \text{ K}, 10^6 \text{ cm}^{-3})$; model 3), is included in the analysis.

To constrain the H_2O excitation, the same physical conditions as determined for CO are taken as fixed and line widths of 40 and 20 km s^{-1} for the *EHV* - *B* and *EHV* - *R* components, respectively, and 50 km s^{-1} for the broad component are adopted. C-type shock models show that CO and H_2O cooling takes place at the same location in a shock (Flower & Pineau des Forêts 2010), thus validating this assumption. The H_2O o/p ratio is assumed to be 3, and the only variable in the RADEX modelling is the total H_2O column density. To constrain this, the ratio of the higher-excited H_2^{16}O lines is taken with respect to the $2_{02}-1_{11}$ line, and the calculated emission in this line is constrained to be greater than the observed value. The same is done for the H_2^{18}O tentative detection and upper limit. A χ^2 analysis is used to determine the best-fit value of the H_2O column density. Once the column density is determined, the predicted intensity is compared to the observed intensity of the $2_{02}-1_{11}$ line, and from this the filling factor is determined. The predicted column density is re-scaled to the average column density in the beam, and compared to $N(\text{CO})$ to determine the $\text{H}_2\text{O}/\text{CO}$ abundance ratio.

The best-fit results are listed in Table 5. $N(\text{H}_2\text{O})$ is found to be $\sim 10^{16}-10^{18} \text{ cm}^{-2}$ for all components and all three models, implying a beam filling factor of $\leq 0.01-0.1$. This leads to an average $\text{H}_2\text{O}/\text{CO}$ abundance ratio of $\sim 0.05-1.0$ in all of the components; the range is caused by the excitation model rather than differences between the physical components. This result is very different from the rotational-diagram analysis above, where the abundance ratio is a factor of > 100 lower. The difference arises because H_2O is not thermalised and optically thick, as opposed to CO , and thus non-LTE, radiative-transfer models are needed to treat the excitation properly. Figure 3 shows the $\text{H}_2\text{O}/\text{CO}$

Table 5. Modelled H_2O line emission and inferred parameters.

	$N(\text{H}_2\text{O})$ (10^{18} cm^{-2}) ^a	χ^2_{red}	$\int T(2_{02}-1_{11}) dv$ (K km s^{-1})	Filling factor ($\times 10^{-3}$)	$\text{H}_2\text{O}/\text{CO}$
Model 1 ^b :					
<i>EHV</i> - <i>B</i>	2.4	0.4	3000	1.3	0.5
<i>EHV</i> - <i>R</i>	0.2	0.4	870	4.4	0.1
Broad	1.2	1.5	2070	8.3	0.3
Model 2 ^c :					
<i>EHV</i> - <i>B</i>	4.0	0.9	2650	1.5	1.0
<i>EHV</i> - <i>R</i>	0.8	0.4	890	4.3	0.5
Model 3 ^d :					
<i>EHV</i> - <i>B</i>	0.8	0.5	3800	1.1	0.1
<i>EHV</i> - <i>R</i>	0.08	0.9	890	4.3	0.05
Broad	0.01	0.2	290	65	0.02

Notes. ^(a) Ortho- + para- H_2O . ^(b) $(T, n) = (150 \text{ K}, 10^6 \text{ cm}^{-3})$ and $(100 \text{ K}, 10^6 \text{ cm}^{-3})$ for the *EHV* and broad components, respectively. ^(c) $(T, n) = (500 \text{ K}, 10^5 \text{ cm}^{-3})$. ^(d) $(T, n) = (500 \text{ K}, 10^6 \text{ cm}^{-3})$ for all components.

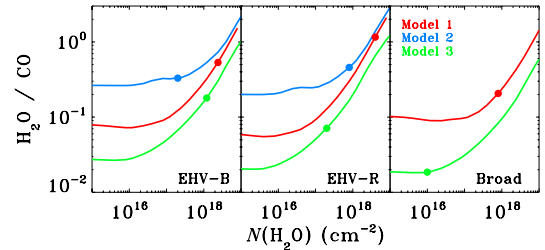


Fig. 3. $\text{H}_2\text{O}/\text{CO}$ ratio as a function of H_2O column density for the three different models 1, 2 and 3. The best-fit results are marked with points.

ratio as function of $N(\text{H}_2\text{O})$ demonstrating that only model 3 produces abundance ratios ≤ 0.1 .

The RADEX models that match the H_2O line emission best predict that the filling factor for the *EHV* component is very small, < 0.01 . Such low values agree with high spatial-resolution observations showing this component to be confined to the molecular jet and consisting of several sub-arcsec knots (e.g., Hirano et al. 2010). The model furthermore predicts that the ground-state transitions have optical depths in excess of 100 (Fig. B.2, Appendix), and that the two H_2^{18}O transitions and the higher-excited H_2^{16}O transitions are also optically thick ($\tau \sim 3-4$). Thus, the optical depth derived from the line ratios can only be considered a relative optical depth between the two transitions. If the H_2^{18}O $1_{10}-1_{01}$ transition is assumed to be optically thin, a typical H_2O column density of a few times 10^{15} cm^{-2} is required. However, models with this column density predict that the intensity of the $2_{02}-1_{11}$ line is close to that observed, or lower in the case of the broad component, implying filling factors of unity inconsistent with the bullet nature. The CO emission remains optically thin ($\tau < 1$) for all three models even with the small filling factors derived for H_2O , consistent with the non-detection of ^{13}CO 3-2.

3.2. Physical origin

3.2.1. *EHV* versus broad components

Following the interpretation of the *EHV* emission in IRAS04191 (Santiago-García et al. 2009) it seems likely that the knots are internal working surfaces (IWS) along the jet that appear as strongly beam-diluted emission in single-dish observations. Regardless of the precise shock details, the high abundance of H_2O in the bullets implies a high H_2 fraction, since otherwise reactions with atomic H drive H_2O back to OH and atomic O.

The timescale for H_2O to be produced in gas as a function of temperature has been determined by Bergin et al. (1998) for $n = 10^5 \text{ cm}^{-3}$. For $T = 500$ K, the timescale is ~ 100 years,

Table 6. H₂O and CO cooling rates in $10^{-3} L_{\odot}$.

		<i>EHV - B</i>	<i>EHV - R</i>	Broad	Total
H ₂ O:	Observed emission	0.4	0.3	1.1	1.8
	Model 1 extrapol.	11.0	4.8	26.6	42.4
	Model 2 extrapol.	10.7	6.4	...	17.1
	Model 3 extrapol.	15.1	6.5	11.7	33.3
CO:	Observed emission	0.2	0.2	0.4	0.8
	T_{ex} extrapol.	1.1	1.1	1.8	4.0

which may be compared to the maximum dynamical time for a bullet with velocity 50 km s^{-1} to leave a beam with radius $11''$, 240 years. Thus, it is possible to reform H₂O from atomic gas over the timescales associated with the bullets. In the lower- T scenario, H₂O will not form in the quantities observed here implying that the temperature is high in the bullets or that H₂O is not formed in the gas phase.

The gas-phase production of H₂O is in agreement with models of continuous spherical wind models of Glassgold et al. (1991), where the formation takes place from a dust-free atomic gas in sufficient quantities if the mass-loss rate exceeds $10^{-5} M_{\odot} \text{ yr}^{-1}$, which is to be compared to the time-averaged mass-loss rate in the jet of $\sim 10^{-6} M_{\odot} \text{ yr}^{-1}$ (Hirano et al. 2010). The mass loss rate traced directly by the bullets is episodic (and thus higher than the time-averaged value) and the wind is not spherical, i.e., it is plausible that the H₂O abundance is consistent with production in the IWS from atomic gas. To resolve the issue of the origin of the molecules and to break the degeneracy between the different models, it is necessary to obtain velocity-resolved data of chemically related species, such as O and OH. Furthermore, measuring the H/H₂ ratio would test the models.

The broad component, centered near v_{LSR} , is now observed in H₂O emission in a number of low-mass sources (Kristensen et al., in prep.). It is interpreted as arising in the interaction between the outflow and envelope, and is seen so prominently in H₂O emission (as opposed to, e.g., CO) due to the high production rate of H₂O at this location. H₂O is formed through both a series of neutral-neutral reactions pushing atomic oxygen into water, and through sputtering of icy grain mantles. Quantifying the contributions from the different mechanisms require observations of other grain-surface products, e.g., CH₃OH, and velocity-resolved observations of the intermediate gas-phase products O and OH. Tafalla et al. (2010) detect CH₃OH emission in both the *EHV* and broad components (but at an outflow position) indicating that a significant fraction of H₂O is sputtered from grains.

3.2.2. Cooling

The observed cooling rate in the three components is found by summing up the observed line emission (Table 6). For the *EHV* components, the H₂O cooling rate is $\sim 3.5 \times 10^{-4} L_{\odot}$, while it is $\sim 1.3 \times 10^{-3} L_{\odot}$ for the broad. Extrapolating the cooling to include all lines with wavelengths greater than $60 \mu\text{m}$ gives a total H₂O luminosity of $2\text{--}4 \times 10^{-2} L_{\odot}$ depending on which model is used (Table 6), i.e., the cooling by the lines observed with HIFI amounts to $\sim 10\%$. The cooling is nearly the same for all three components demonstrating the power of spectrally resolving line profiles. This number may be compared to $4.5 \times 10^{-2} L_{\odot}$ as was found for H₂O by ISO-LWS in an $80''$ beam (Nisini et al. 2000), which applies to the sum of the components.

The observed CO cooling rate is somewhat higher, $\sim 2 \times 10^{-3}$ and $6.0 \times 10^{-3} L_{\odot}$, respectively. The CO cooling rate for the three components is extrapolated using the rotational diagrams to a

total of $4.0 \times 10^{-3} L_{\odot}$, lower than the H₂O cooling. The *EHV* components contribute $\sim 50\%$ to the CO cooling. ISO-LWS observed a total CO cooling rate of $3.0 \times 10^{-2} L_{\odot}$ (Nisini et al. 2000), but in a much larger beam encompassing the extended outflow emission and other physical components (van Kempen et al. 2010).

4. Conclusions

H₂O emission readily traces the *EHV* gas that has previously only been seen in very deep integrations of other species, such as CO. The *EHV* components are attributed to shocks in the molecular jet, while the underlying broad component, now seen in several low-mass YSOs, is associated with the interaction of the outflow and the envelope on larger scales. Thus, HIFI and H₂O together are ideal for revealing the dynamical components of low-mass star-forming regions. Both components are H₂ rich, since otherwise the H₂O abundance would be lower. The two distinct components appear remarkably similar in terms of excitation and chemical conditions in spite of their different chemistries. They have equal contributions from H₂O and CO cooling with H₂O being the dominant coolant of the two. High spectral-resolution observations are a prerequisite for interpreting spectrally unresolved PACS data of the same source.

Acknowledgements. HIFI has been designed and built by a consortium of institutes and university departments from across Europe, Canada and the US under the leadership of SRON Netherlands Institute for Space Research, Groningen, The Netherlands with major contributions from Germany, France and the US. Consortium members are: Canada: CSA, U. Waterloo; France: CESR, LAB, LERMA, IRAM; Germany: KOSMA, MPIfR, MPS; Ireland, NUI Maynooth; Italy: ASI, IFSI-INAf, Arcetri-INAf; Netherlands: SRON, TUD; Poland: CAMK, CBK; Spain: Observatorio Astronómico Nacional (IGN), Centro de Astrobiología (CSIC-INTA); Sweden: Chalmers University of Technology – MC2, RSS & GARD, Onsala Space Observatory, Swedish National Space Board, Stockholm University – Stockholm Observatory; Switzerland: ETH Zürich, FHNW; USA: Caltech, JPL, NHSC. Astrochemistry in Leiden is supported by NOVA, by a Spinoza grant and grant 614.001.008 from NWO, and by EU FP7 grant 238258. The WISH team is thanked for stimulating discussions.

References

- Arce, H. G., et al. 2007, in *Protostars and Planets V*, ed. B. Reipurth, D. Jewitt, & K. Keil, 245
- Bachiller, R., et al. 1990, *A&A*, 231, 174
- Bergin, E. A., Neufeld, D. A., & Melnick, G. J. 1998, *ApJ*, 499, 777
- de Graauw, T., Helmich, F. P., Phillips, T. G., et al. 2010, *A&A*, 518, L6
- Faure, A., Crimier, N., Ceccarelli, C., et al. 2007, *A&A*, 472, 1029
- Flower, D. R., & Pineau des Forêts, G. 2010, *MNRAS*, 406, 1745
- Franklin, J., Snell, R. L., Kaufman, M. J., et al. 2008, *ApJ*, 674, 1015
- Glassgold, A. E., Mamon, G. A., & Huggins, P. J. 1991, *ApJ*, 373, 254
- Guilloteau, S., Bachiller, R., Fuente, A., & Lucas, R. 1992, *A&A*, 265, L49
- Hirano, N., Ho, P. P. T., Liu, S., et al. 2010, *ApJ*, 717, 58
- Kristensen, L. E., Visser, R., van Dishoeck, E. F., et al. 2010, *A&A*, 521, L30
- Lefloch, B., Cabrit, S., Codella, C., et al. 2010, *A&A*, 518, L113
- Nisini, B., Benedettini, M., Giannini, T., et al. 1999, *A&A*, 350, 529
- Nisini, B., Benedettini, M., Giannini, T., et al. 2000, *A&A*, 360, 297
- Nisini, B., Codella, C., Giannini, T., et al. 2007, *A&A*, 462, 163
- Pickett, H. M., et al. 1998, *J. Quant. Spectroscopy and Radiative Transfer*, 60, 883
- Pilbratt, G. L., Riedinger, J. R., Passvogel, T., et al. 2010, *A&A*, 518, L1
- Santiago-García, J., et al. 2009, *A&A*, 495, 169
- Tafalla, M., et al. 2010, *A&A*, 522, A91
- van der Tak, F. F. S., et al. 2007, *A&A*, 468, 627
- van Dishoeck, E. F., Kristensen, L. E., Benz, A. O., et al. 2011, *PASP*, 123, 138
- van Kempen, T., Kristensen, L., Herczeg, G., et al. 2010, *A&A*, 518, L121
- Yang, B., Stancil, P. C., Balakrishnan, N., & Forrey, R. C. 2010, *ApJ*, 718, 1062
- Yıldız, U. A., van Dishoeck, E. F., Kristensen, L. E., et al. 2010, *A&A*, 521, L40

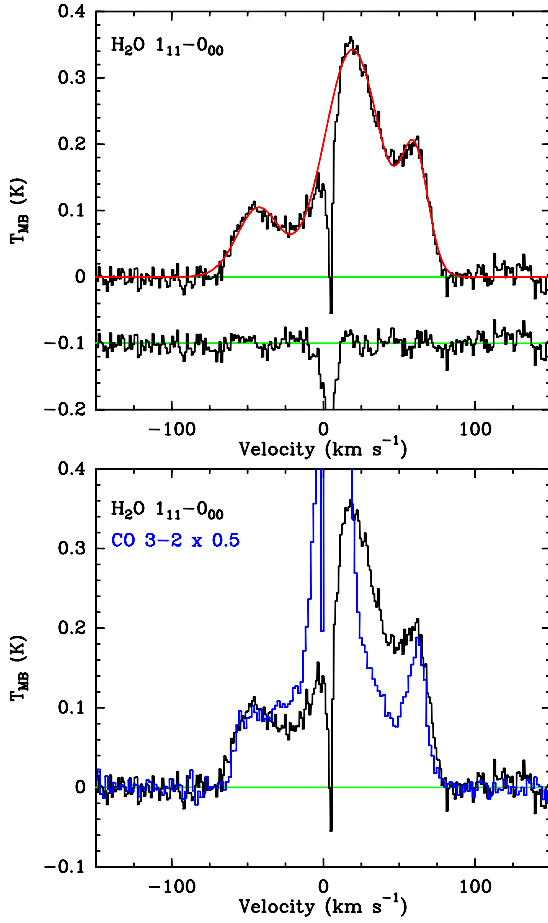


Fig. A.1. *Top:* Gauss fit of the $\text{H}_2\text{O } 1_{11}-0_{00}$ line (red) with the residual shown below (offset at -0.1 K). The central absorption feature is not fitted. *Bottom:* CO 3–2 scaled to the peak intensity of H_2O in the bullets and overlotted on the $\text{H}_2\text{O } 1_{11}-0_{00}$ line.

Appendix A: Gauss fit of data

The data are fitted by Gaussians, with the exception of the narrow absorption component. Figure A.1 shows the example of the $\text{H}_2\text{O } 1_{11}-0_{00}$ line, with the residual plotted below. Furthermore, Fig. A.1 shows the CO 3–2 line scaled and overlotted on the $\text{H}_2\text{O } 1_{11}-0_{00}$ line, highlighting the similar line profile in the *EHV* components.

Appendix B: RADEX results

The non-LTE, escape-probability code RADEX was used to create rotational diagrams for H_2O and CO in the optically thin limit. Collisional rate coefficients are from Faure et al. (2007) and Yang et al. (2010), respectively. The same transitions as observed were then used to calculate the rotational temperature as function of T_{kin} and n_{H} . The results are shown in Fig. B.1.

RADEX was also used to calculate the optical depth, τ of the $\text{H}_2^{16}\text{O } 1_{10}-1_{01}$ line at 557 GHz. Results are shown in Fig. B.2, where also the beam-filling factor is shown as a function of H_2O column density for the three different models.

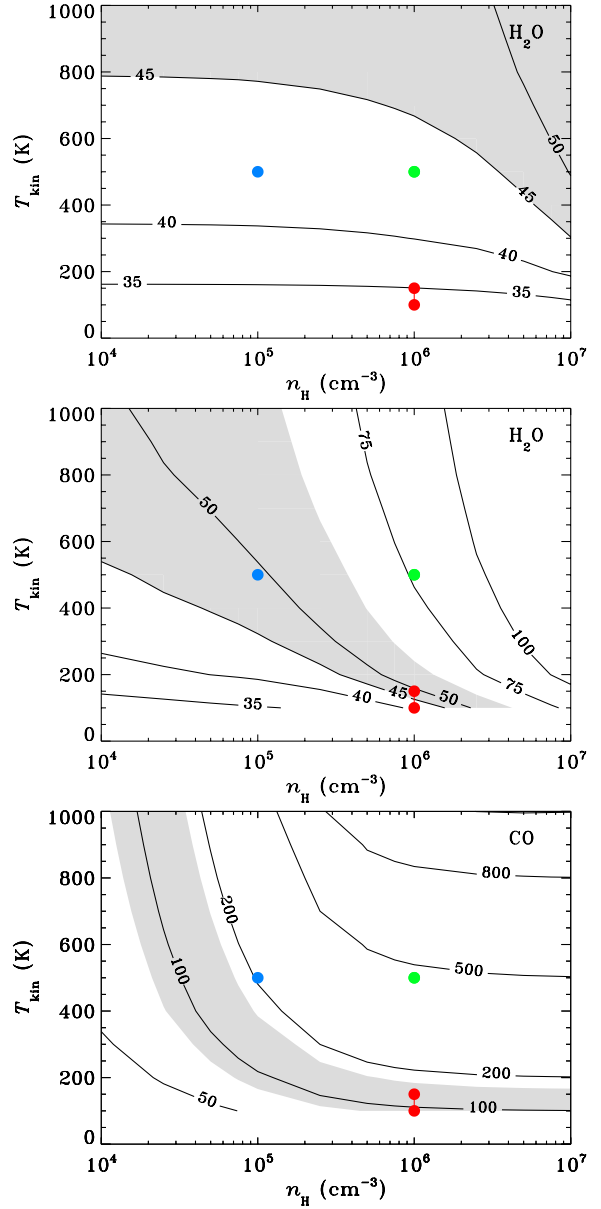


Fig. B.1. T_{rot} of optically thin H_2O emission (*top*), optically thick H_2O emission ($N = 10^{17} \text{ cm}^{-2}$; *middle*) and optically thin CO emission (*bottom*) determined from RADEX simulations. T_{rot} is calculated from the same transitions as in Sect. 2, i.e., excluding the ground-state transitions. The gray area indicates the observed values of T_{rot} . The points indicate the different physical conditions examined; model 1 (red) has $(T, n) = (150 \text{ K}, 10^6 \text{ cm}^{-3})$ for the *EHV* components and $(100 \text{ K}, 10^6 \text{ cm}^{-3})$ for the broad component. Model 2 (blue) has $(T, n) = (500 \text{ K}, 10^5 \text{ cm}^{-3})$ for the *EHV* components, respectively. Model 3 (green) has $(T, n) = (500 \text{ K}, 10^6 \text{ cm}^{-3})$ for all components.

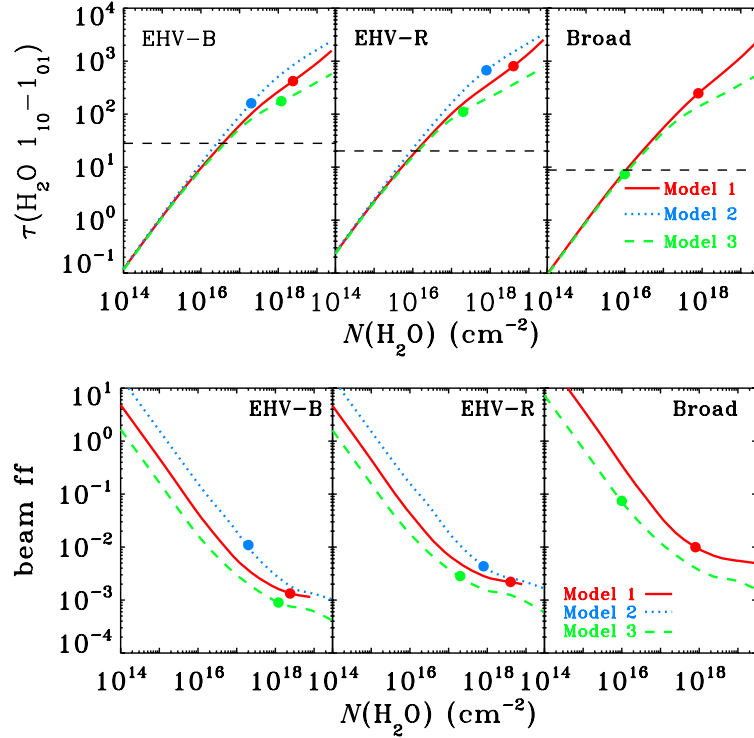


Fig. B.2. *Top:* τ of the H_2^{16}O $1_{10}-1_{01}$ line. The black dashed line corresponds to the observed value in each of the three velocity components as specified in Sect. 2. *Bottom:* beam-filling factor for the three different components and three different models as a function of total H_2O column density. Best-fit results are marked with points in both plots.

Table 2. H_2O , H_2^{18}O and CO emission in each velocity component at the source position^a.

Transition	rms ^b (mK)	EHV - B				EHV - R				Broad			
		$T_{\text{MB}}^{\text{peak}}$ (mK)	$\int T_{\text{MB}} dv$ (K km s ⁻¹)	FWHM (km s ⁻¹)	v_{LSR} (km s ⁻¹)	$T_{\text{MB}}^{\text{peak}}$ (mK)	$\int T_{\text{MB}} dv$ (K km s ⁻¹)	FWHM (km s ⁻¹)	v_{LSR} (km s ⁻¹)	$T_{\text{MB}}^{\text{peak}}$ (mK)	$\int T_{\text{MB}} dv$ (K km s ⁻¹)	FWHM (km s ⁻¹)	v_{LSR} (km s ⁻¹)
H_2O $1_{10}-1_{01}$	9	74	2.54	32.3	-44.2	122	3.00	23.0	60.1	294	14.40	46.0	14.0
$1_{11}-0_{00}$	11	101	3.98	37.1	-41.1	176	4.00	21.3	60.1	337	14.76	41.2	20.1
$2_{02}-1_{11}$	14	93	4.01	40.3	-43.7	175	3.86	20.7	59.8	328	17.59	50.4	18.0
$2_{11}-2_{02}$	14	65	2.47	35.9	-44.2	109	2.53	21.9	60.0	207	9.91	44.9	15.4
$3_{12}-3_{03}$	13	50	2.34	44.0	-45.4	65	1.14	16.5	60.7	124	7.76	54.5	16.3
$3_{12}-2_{21}$	66	147	6.22	39.7	-43.1	111	3.32	28.1	55.4	139	7.94	53.4	14.8
H_2^{18}O $1_{10}-1_{01}$ ^c	3	4	0.13	5	0.11	5	0.23
$1_{11}-0_{00}$ ^d	11	...	<0.25	<0.19	<0.28
CO 2-1	51	184	2.79	14.2	-51.6	280	4.12	13.8	60.3	498	38.53	72.8	0.8
3-2	39	216	4.82	21.0	-48.2	467	6.58	13.2	61.9	657	44.85	64.1	8.0
4-3	160	467	11.9	24.0	-45.1	808	15.1	17.5	65.7	1023	74.61	68.5	19.0
10-9	66	269	7.30	25.5	-47.2	426	8.42	18.6	61.3	323	17.77	51.6	10.1

Notes. ^(a) Obtained from Gaussian fits to each component. ^(b) Measured in 1 km s⁻¹ bins. ^(c) Obtained by fixing the position and width of Gaussian functions to the average value and only fitting the intensity. ^(d) Upper limits are 3σ .

Table 3. H_2O , H_2^{18}O and CO transitions observed with *Herschel*-HIFI^a.

Transition	ν (GHz)	λ (μm)	E_u/k_B (K)	A (10^{-3} s^{-1})	Beam ($''$)	t_{int}^b (min.)	η_{MB}
H_2O $1_{10}-1_{01}$	556.94	538.29	61.0	3.46	39	13.0	0.74
$1_{11}-0_{00}$	1113.34	269.27	53.4	18.42	19	43.5	0.75
$2_{02}-1_{11}$	987.93	303.46	100.8	5.84	22	23.3	0.73
$2_{11}-2_{02}$	752.03	398.64	136.9	7.06	29	18.4	0.74
$3_{12}-3_{03}$	1097.37	273.19	249.4	16.48	20	32.4	0.75
$3_{12}-2_{21}$	1153.13	259.98	249.4	2.63	19	13.0	0.65
H_2^{18}O $1_{10}-1_{01}$	547.68	547.39	60.5	3.59	39	64.3	0.74
$1_{11}-0_{00}$ ^c	1101.70	272.12	52.9	21.27	20	43.5	0.75
CO 10-9	1151.99	260.24	304.1	0.10	19	13.0	0.65

Notes. ^(a) From the JPL database of molecular spectroscopy (Pickett et al. 1998). ^(b) Total on + off + overhead integration time. ^(c) Observed in the same setting as the main isotopologue.